PAPER

The thermoelastic properties of monolayer covalent organic frameworks studied by machine-learning molecular dynamics†

Bing Wang, Penghua Ying ‡ and Jin Zhang *

Two-dimensional (2D) covalent organic frameworks (COFs) are emerging as promising 2D polymeric materials with broad applications owing to their unique properties, among which the mechanical properties are quite important for various applications. However, the mechanical properties of 2D COFs have not been systematically studied yet. Herein, a machine-learned neuroevolution potential (NEP) was developed to study the elastic properties of two representative monolayer 2D COFs, namely COF-1 and COF-5. The trained NEP enables one to study the elastic properties of 2D COFs in realistic situations (*e.g.,* finite size and temperature) and possesses greatly improved computational efficiency when compared with density functional theory calculations. With the aid of the obtained NEP, molecular dynamics (MD) simulations together with a strain-fluctuation method were employed to evaluate the elastic constants of the considered 2D COFs at different temperatures. The elastic constants of COF-1 and COF-5 monolayers were found to decrease with an increase in the temperature, though they were almost isotropic irrespective of the temperature. The thermally induced softening of 2D COFs below a critical temperature was observed, which is mainly attributed to their inherent ripple configurations at finite temperatures, while above the critical temperature, the damping effect of anharmonic vibrations became the dominant factor. Based on the proposed mechanisms, analytical models were developed for capturing the temperature dependence of elastic constants, which were found to agree with the MD simulation results well. This work provides an in-depth insight into the thermoelastic properties of monolayer COFs, which can guide the development of 2D COF materials with tailored mechanical behaviors for enhancing their performance in various applications.

Introduction

In recent years, covalent organic frameworks (COFs) have emerged as a highly promising class of crystalline porous polymers, which possess unique structures that are composed of a network of dynamic covalent bonds.[1] Owing to their unique structures, COFs possess a large void space and a high surface area, which render them the capacity to be used in adsorbing and separating hydrogen, carbon dioxide, methane, and other gases.[2–4] Besides, COFs are promising catalytic platforms owing to their abundant and uniform open channels, as well as their excellent insolubility and high stability. These characteristics are crucial for facilitating the mass-transfer process in catalysis.[5,6] The highly efficient size selectivity of COFs due to

their uniform pores has also led to them being employed as highly efficient and size-selective catalysts.[7] Meanwhile, COFs have been designed for use as potential Li-ion solid-state conductors and in flexible electronics, since most of them are flexible and have high conductivities, including thermal conductivity, among the reported crystalline porous materials.[8–10]

Among the different types of COFs, two-dimensional (2D) COFs are currently receiving much attention because of their unique structural properties. Each individual layer in 2D COFs maintains its in-plane stability through strong covalent bonds, while neighboring layer components are connected with each other *via* weak interlamellar interactions. The inherent structure of 2D COFs allows the precise manipulation and customization of their pores at a nanoscale level.[11] As a result, 2D COFs can be designed with multi-level porosity, which makes them possibly exhibit an excellent performance in the applications of adsorption and catalysis and in the manufacture of micro/nanodevices.[12,13] Specifically, the most practical applications of 2D COFs strongly rely on their mechanical properties because previous studies indicate that the physical and chemical properties of 2D materials and COFs can be signifi-

School of Science, Harbin Institute of Technology, Shenzhen 518055, PR China.
E-mail: jinzhang@hit.edu.cn

†Electronic supplementary information (ESI) available. See DOI: https://doi.org/10.1039/d3nr04509a

‡Present address: Department of Physical Chemistry, School of Chemistry, Tel Aviv University, Tel Aviv, 6997801, Israel.

cantly affected by mechanical stimuli.[14] Thus, strain engineering is an effective method to modify the size of pores in 2D materials, allowing the separation of different gas mixtures at a specific pore size[15] and changes in water permeability for 2D materials.[16] Similarly, the thermal conductivity of COFs can be effectively modulated through strain engineering.[17,18] Besides, mechanical stimuli are also inevitable in many applications of 2D materials. For instance, in the thermal catalysis applications of 2D materials, such as 2D MXenes, the operational conditions typically encompass elevated temperatures and pressures. The catalytic efficacy is notably contingent upon the thermodynamic and mechanical robustness of 2D MXenes.[19] In the manufacture and application of nanosensors, stable mechanical performance of the component 2D films is crucial for the production and reusability of these devices.[20] However, even though the mechanical property of 2D COFs is a fundamental intrinsic feature relevant to most of their applications, there are relatively few reports on their mechanical behaviors.

In spite of two very recent experimental reports on the tensile properties of multilayer COFs,[21,22] atomistic simulations including density functional theory (DFT) calculations and molecular dynamics (MD) simulations are generally employed to investigate the mechanical properties of 2D COFs. By using DFT calculations, Kapri et al.[23] calculated the elastic tensor of some 2D COFs very recently. Although the DFT approach has high accuracy, it is computationally expensive, and it is thus difficult to use DFT for studying COFs with large pores or complex structures. Moreover, it is usually difficult to consider the effects of the crystal size and finite temperature in DFT calculations. To overcome the limitations of DFT calculations, MD simulations are usually treated as a more effective method for theoretically studying the mechanical behaviors of 2D COFs. By exploiting MD simulations, Zhang[24] reported a phase transition occurring in 2D COFs due to compression. The phase transition was found to have an effect on the elastic constants, band gap, and thermal conductivity of the studied 2D COFs. Li and Brédas[25] reported the elastic properties of COFs using OPLS all-atom force field potentials[26] and pointed out that the existence of structural defects will significantly reduce the stiffness of 2D COFs. Very recently, Hao et al.[27] revealed that 2D COFs possess a superior impact-resistant capability under high-velocity impacts. Although these initial results reveal some fundamental mechanical characters of 2D COFs, there still exist some limitations in these MD studies. For example, these studies were based on some empirical potentials specifically developed for other materials rather than COFs.[25,28] Thus, the accuracy of these empirical potentials in describing 2D COFs may be questionable. Recently, machine-learned potential (MLP) has been shown to be a promising on-demand approach for investigating the mechanical properties of 2D materials.[29] For example, machine-learning interatomic potentials (MLIPs) were developed by Mortazavi et al. for studying the mechanical behaviors and properties of various 2D materials.[30,31] It was shown that MLIPs could enable the efficient use of classical MD simulations to evaluate the mechanical properties of relatively large

2D material systems with the DFT level of accuracy. Moreover, the MLIPs also enable first-principles multiscale modeling, in which the DFT level of accuracy can be hierarchically bridged to explore the mechanical properties of macroscopic 2D material systems.[32] Also, Ying et al. very recently employed MLPs to investigate the mechanical responses of a monolayer quasi-hexagonal-phase fullerene membrane subjected to uniaxial tension.[33] Overall, the MLPs developed recently provide a possible avenue for studying the mechanical properties of 2D COFs that possess large pores and abundant elements.

Motivated by these ideas and previous studies, in this work we developed neuroevolution potential (NEP) framework-based MLPs[34] for two representative 2D COFs, namely COF-1 and COF-5.[1] The obtained NEP was further applied to investigate the elastic properties of the monolayer COFs at different temperatures by using extensive MD simulations together with the strain-fluctuation method.[35,36] Here, we considered the monolayers of these 2D COFs because many monolayer COFs have been successfully synthesized recently and have been found to exhibit many unique properties and possess many potential applications.[37–39] Moreover, a comprehensive understanding of the elastic property of their component layer is also a necessary first step toward understanding the elastic property of layered 2D COFs. Our results show that the temperature generally has a softening effect on the elasticity of monolayer COFs, although the temperature sensitivity of the elastic constants is different below and above a critical temperature. In particular, the greater softening effect observed below the critical temperature can be majorly attributed to the thermal rippling of monolayer COFs, while the increased nonharmonic forces above the critical temperature can suppress the effect of thermal rippling, resulting in a lower sensitivity of the elastic moduli to temperature. Based on the proposed mechanisms, some analytical models were developed for better capturing the temperature dependence of the elastic constants of monolayer 2D COFs.

Simulation models and methods

Simulation models

In this study, we focused on two typical monolayer COFs, i.e., COF-1 and COF-5, which were assembled through reactions between organic precursors, resulting in strong covalent bonds to afford porous, stable, and crystalline materials. Specifically, as shown in Fig. 1a, COF-1 was composed of the building blocks of benzene-1,3,5-tricarboxylic acid (BTC) and 1,3,5-tris (4-aminophenyl) benzene (TAPB), while COF-5 contained the building blocks of 1,4-benzenedicarboxylic acid (BDC) and 1,2-bis (4-pyridyl) ethylene (BPE). MD simulations were employed to study the elastic behaviors of the aforementioned monolayer 2D COF materials. It is known that the elastic properties, especially the elastic moduli, rely on the size of the structures considered in MD simulations, and the elastic modulus could be wrongly estimated if the size of the simulated system is too small.[40] Therefore, to ensure the accuracy of the simulation results, we chose a relatively large size of 40.7 nm × 39.1 nm
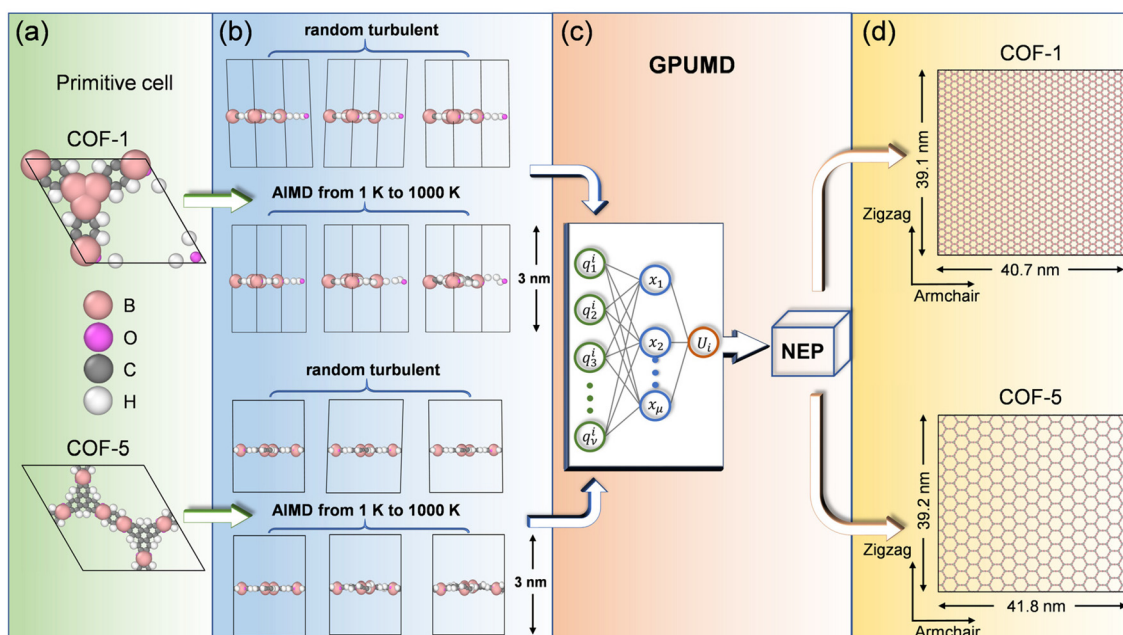
Fig. 1 Workflow for training the NEP model for 2D COF monolayers. (a) Primitive cells of COF-1 and COF-5. (b) Construction of the training and testing data sets. (c) Schematic of the NEP frameworks. (d) Supercells of the monolayer COF-1 and COF-5 used to evaluate their elastic properties. The OVITO package was used here for visualization.[41]

for COF-1, which consisted of 31 500 atoms, and a size of 41.8 nm × 39.2 nm for COF-5, which contained 19 968 atoms. As shown in Fig. S1 in the ESI,† a convergence of the Young's modulus was observed after the length of the COF-1 and COF-5 models was larger than 25 nm, indicating the suitability of the size of 2D COFs selected here. In our simulations, a vacuum spacing of 3 nm was placed in the out-of-plane direction to avoid non-physical interactions between the COF layer and its replicas, while periodic boundaries were employed in the in-plane directions.

Acquisition of dataset from first-principles calculations

As illustrated in Fig. 1b, 2400 structures were constructed in total for training and testing the NEP model, which were equally comprised of structures of COF-1 and COF-5. Moreover, 2000 structures were extracted from *ab initio* molecular dynamics (AIMD) simulations, while the other 400 structures were obtained by manual perturbations. All the structures in the reference dataset were based on the primitive cells of monolayer COF-1 and COF-5. In the AIMD simulations, the structural sampling was performed under the NVT ensemble with a Nosé–Hoover heat bath,[42] in which the system temperature was linearly raised from 1 K to 1000 K within 10 ps. Here, the time step was set as 1 fs. The perturbated structures were obtained by randomly adding 5% perturbations to the lattice constants and changing the atomic coordinates with a distance less than 0.2 Å. With the structures of COF-1 and COF-5 established through the aforementioned process, we calculated their energy, virial, and atomic force using single-point DFT calculations. All the DFT calculations and AIMD simulations were implemented by the VASP

package[43,44] with the Perdew–Burke–Ernzerhof functional.[45] The electronic self-consistent loop was set at a threshold of 10^{-7} eV, while an energy cutoff of 800 eV was utilized. The k-point grid was set as $2 \times 2 \times 1$. The suitability of the energy cutoff and wave-vector grid could be verified by the fact that the converged energy of the system was observed at the selected energy cutoff and wave-vector grid, as shown in Fig. S2.†

Training of the NEP framework for monolayer COFs

The MLP model based on the third-generation NEP framework[46] was trained with the aid of using the GPUMD package.[47] The workflow is briefly shown in Fig. 1c. Here, we randomly divided the total dataset into a training dataset and a testing dataset in a ratio of 4 : 1. In order to train the NEP potential for the considered monolayer 2D COFs, several hyperparameters needed to be set. The hyperparameters used for testing can be found in the ESI (Table S1†). The impact of various hyperparameters on the accuracy of the NEP model was thoroughly evaluated. Specifically, the cutoff radii for the radial and angular descriptor components were $r_c^R = 10$ Å and $r_c^A = 4$ Å, respectively. The Chebyshev polynomial expansion orders for the radial and angular descriptor components were $n_{max}^R = 6$ and $n_{max}^A = 4$. The suitability of the selected hyperparameters was confirmed by the results shown in Fig. S3.† Moreover, the Legendre polynomial expansion order for the angular descriptor components was $l_{max} = 4$. Besides, we employed 100 neurons in the hidden layer of the neural network. The default setting was used for the normalized factors of λ_1, λ_2, λ_e, λ_f, and λ_v, which were 0.1, 0.1, 1.0, 1.0, and 0.1, respectively. The population size and the number of gener-

ations in the algorithm were $N_{pop} = 50$ and $N_{gen} = 5 \times 10^6$, respectively. After determining the aforementioned hyperparameters, we could finally get an NEP function for both the COF-1 and COF-5 monolayers.

Strain-fluctuation methods

The NEP model obtained above was employed in MD simulations for further evaluating the elastic properties of the monolayer COF-1 and COF-5 at the finite temperature, which was implemented by the strain-fluctuation method.[35,36] The strain-fluctuation method calculates the elastic constants by examining strain fluctuations in a thermally equilibrated system without applying any stimuli. Furthermore, all the components of the elastic tensor can be calculated in a single simulation. This method is predicated on the fluctuation-dissipation theorem that relies on the assumption that spontaneous fluctuations and small mechanical stimuli will generate the similar responses of a system in thermodynamic equilibrium.[48] Besides the strain-fluctuation method, the stress-fluctuation method is another method based on the fluctuation-dissipation theorem, which also has the capability to calculate the elastic constants of materials at a specific temperature. Nevertheless, the implementation of the stress-fluctuation method is more rigorous and complex, especially for atomic models involving intramolecular interactions.[49] Therefore, we chose the strain-fluctuation method here to conduct the thermodynamic statistics tests for the 2D COF structures at a constant temperature and ambient pressure (NPT ensemble), which were further used to calculate the elastic constants for the 2D COFs.

To implement the calculations based on the strain-fluctuation method, all the 2D COF structures were relaxed for 1000 ps at 0 GPa in the NPT ensemble by using the stochastic cell rescaling method,[50] which makes the structures reach their equilibrium at a certain temperature. In all the simulations, the strain ε_{ij} was determined from the following equation:[35,36]

$$\varepsilon_{ij} = \frac{1}{2}\left[\langle h\rangle_{ik}^{-T} h_{kl}^T h_{lm}\langle h\rangle_{mj}^{-1} - \delta_{ij}\right]. \quad (1)$$

where $h_{ij} = \{a, b, c\}_{ij}$ is a matrix with components of principal axes (a, b, and c) of the simulation box, which can be extracted from MD simulations and also has the ability to describe the size and shape of the simulation box. The matrix $\langle h\rangle_{ij}$ describes the average shape of the system as the reference state. Also, $\langle h\rangle_{ij}^{-T}$ is the inverse of the transpose of $\langle h\rangle_{ij}$, and δ_{ij} is the Kronecker tensor. The full second-order compliance tensor S at the temperature T and pressure P was then obtained as:[36]

$$S_{\alpha\beta\gamma\kappa} = \frac{\langle V\rangle}{k_B T}\text{cov}(\varepsilon_{\alpha\beta}(t),\varepsilon_{\gamma\kappa}(t))$$
$$= \frac{\langle V\rangle}{k_B T}\langle(\varepsilon_{\alpha\beta}(t) - \langle\varepsilon_{\alpha\beta}\rangle)(\varepsilon_{\gamma\kappa}(t) - \langle\varepsilon_{\gamma\kappa}\rangle)\rangle, \quad (2)$$

where k_B is the Boltzmann constant, $\varepsilon_{\alpha\beta}(t)$ [or $\varepsilon_{\gamma\kappa}(t)$] is the strain at the time of t, and $\langle V\rangle$ describes the average of volume.

Here, the layer thickness was set as 3.34 Å in the calculations of the volumes of the monolayer COFs, which equals their van der Waals distances.[51,52] Based on the compliance tensor S extracted above, we can finally calculate the second-order stiffness tensor C by inversing the matrix S, i.e., $C = S^{-1}$.

The result in Fig. S4† shows the evolution of the elastic constants with respect to the simulation time, which indicated a convergency of the elastic stiffness tensors after the simulation for 1000 ps. Thus, the unit cell vector was output in another successive simulation with 500 ps, which was further divided into five groups. The average of the compliance tensors of these five groups was treated as the final result, while the standard error of the five groups of data was regarded as the calculation error.

Results and discussion

Validation of the NEP model for COF-1 and COF-5

In Fig. 2a and b, we show the evolution of the loss functions for the training dataset of the considered monolayer 2D COFs with respect to the generations. All the loss functions were found to become completely converged when the training was performed after 10^6 generations. The corresponding energy, force, and virial of the monolayer COFs predicted by NEP were also compared against the corresponding DFT results in Fig. 2. Here, the extremely small values of the root-mean square (RMS) error for the energy, force, and virial indicate that the NEP model trained here was capable of accurately predicting the energy, force, and virial properties of the monolayer COFs considered here.
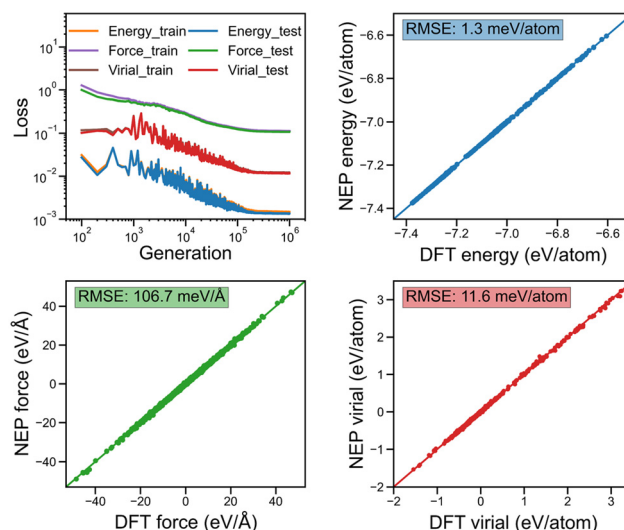

Fig. 2 The evolution of various loss functions for the training and testing dataset with respect to the generation together with the corresponding energy, force, and virial obtained from the NEP compared to the values obtained from DFT calculations for both the training and testing datasets of COF-1 and COF-5.

To evaluate the accuracy of the trained NEP model in describing the structures of the 2D COFs considered in the MD simulations, we compared the radial distribution function (RDF) of COF-1 and COF-5 obtained from the NEP-based MD and AIMD simulations at 300 K. As shown in Fig. 3, a good agreement was observed between these two methods, indicating that the NEP model could faithfully capture the structural characteristics of the monolayer COF-1 and COF-5.

To further validate the precision of NEP in evaluating the elastic properties of the monolayer COF-1 and COF-5, we compared the energy changes in the strained 2D COFs extracted from NEP-based MD simulations and DFT calculations. Here, all the DFT calculation results were based on the primitive cells as shown in the inset of Fig. 4, while all the NEP calculations were based on $5 \times 5 \times 1$ supercells. In addition, the strain was defined as the relative changes of the lattice con-
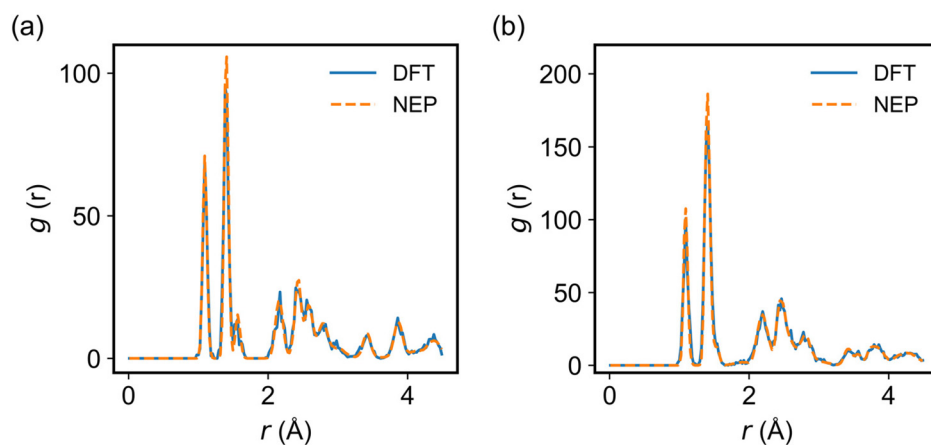

Fig. 3 The RDFs of (a) COF-1 and (b) COF-5 calculated by using classical MD simulations at 300 K driven by DFT (solid lines) and NEP (dashed lines).
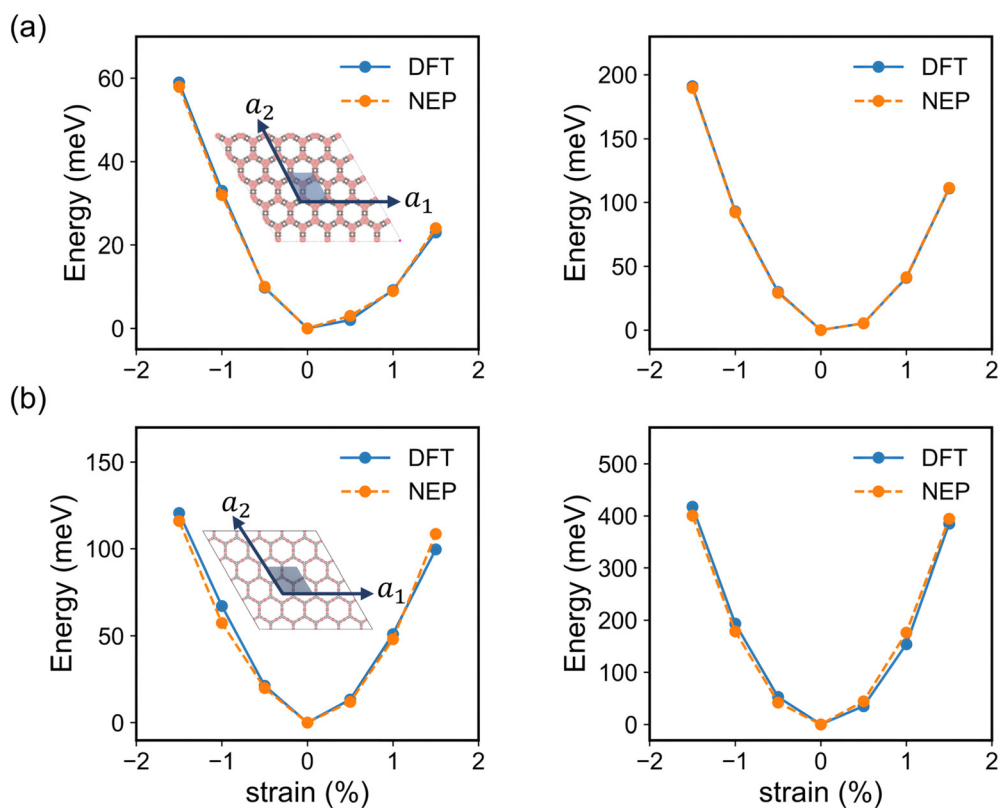

Fig. 4 The energy changes in the primitive cells of (a) COF-1 and (b) COF-5 with strain applied only along the lattice vector a_1 (left) and along both a_1 and a_2 lattice vectors (right), which were obtained by using both DFT and NEP calculations. The insets show the crystal structures of monolayer COF-1 and COF-5, where the primitive cells are indicated by blue parallelograms.

stants in the strained monolayer.[53] As shown in the inset of Fig. 4, the strain was applied along the lattice vector a_1 to represent the uniaxial deformation and along both a_1 and a_2 lattice vectors to represent the biaxial deformation condition to the monolayer COFs. As shown in Fig. 4, the energy changes in both the strained COF-1 and COF-5 monolayers obtained from DFT calculations were identical to the results calculated by the NEP models. We further employed the energy-strain method to calculate the elastic constants of the 2D COFs, which was implemented by VASPKIT.[54] In this method, the elastic stiffness tensor is derived from the second-order derivative of the energy change with respect to the applied strain.[55] Since the monolayer COF-1 and COF-5 considered here possessed 2D hexagonal structures, only three independent elastic constants, i.e., C_{11}, C_{12}, and C_{66} were calculated. These independent components of the elastic stiffness tensor calculated from NEP models are summarized in Table 1, in comparison with the corresponding DFT results. As for all elastic constants of monolayer COF-1 and COF-5, the error between the NEP and DFT results was within 1.2%. This good agreement demonstrates the accuracy of the trained NEP model for evaluating the elastic properties of the considered 2D COFs.

Thermoelastic properties of monolayer COFs

Apart from the high computational cost, DFT calculations usually are only available for calculating the elastic constants of a material at the zero-temperature ground state.

Table 1 The elastic constants of COF-1 and COF-5 monolayers obtained from NEP models and DFT calculations

Elastic constant (GPa)	COF-1		COF-5	
	NEP	DFT	NEP	DFT
C_{11}	81.8	82.6	57.2	57.4
C_{12}	66.0	66.0	48.6	48.7
C_{66}	8.2	8.1	4.3	4.3

Nevertheless, as the temperature increases, the atoms of a material vibrate more vigorously, resulting in thermal expansion and changes in the elastic properties of materials. Therefore, when studying the elastic properties of a material at finite temperatures, it becomes necessary to take into account some additional factors, such as the thermal effect and anharmonic contributions.[56,57]

In this study, we employed the strain-fluctuation method to calculate the elastic constants of monolayer COF-1 and COF-5 over a temperature range from 10 K to 500 K. Here, the interval was 10 K for the temperature increasing from 10 to 100 K, while it was 50 K for the temperature largely growing from 100 to 500 K. The thermodynamical stability of these monolayer COFs at high temperatures could be verified by the stability of their energy during AIMD simulations in the NVT ensemble (Fig. S3†). Fig. 5 illustrates the temperature-dependent variations in the elastic constants C_{11}, C_{12}, and C_{66}. For monolayer COF-1, a significant decrease was observed in both C_{11} and C_{12} at temperatures below 60 K. Specifically, as the temperature increased from 0 to 60 K, C_{11} of COF-1 decreased from 81.8 to 7.3 GPa, while its C_{12} decreased from 66.0 to −2.27 GPa. In the similar process, a much smaller change was observed in C_{66}, which only declined from 8.2 to 4.2 GPa. However, when the temperature was larger than 60 K, the changes in the elastic constants became much slighter. As shown in Fig. 5a, when the temperature increased from 60 to 500 K, the $C11$ of COF-1 only decreased from 7.4 to 4.6 GPa, while its $C12$ and C_{66} fluctuated within small ranges, which were, respectively, −5.9 to 1.9 GPa and 1.7 to 7.3 GPa.

A similar trend was observed in the elastic constants of COF-5 at different temperatures. As depicted in Fig. 5b, when the temperature increased from 0 to 40 K, C_{11} and C_{12} of COF-5 decreased from 57.3 to 7.1 GPa and from 48.6 to −0.6 GPa. In this process, C_{66} of COF-5 slightly decreased from 3.8 to 3.5 GPa. When the temperature further grew from 40 to 500 K, a decrease with a much smaller rate was observed in $C11$ of COF-5, which decreased from 7.1 to 4.0 GPa. Now, its $C12$ and C_{66} remained relatively stable, fluctuating from −1.6
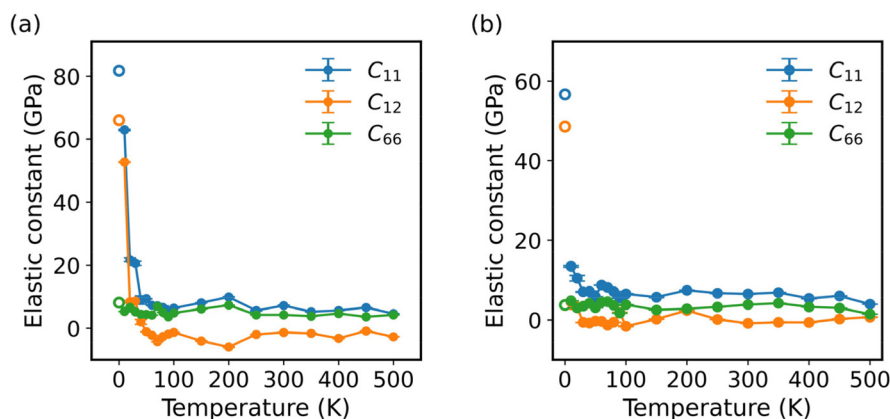

Fig. 5 The elastic constants of (a) COF-1 and (b) COF-5 at different temperatures ranging from 0 to 500 K. The hollow circles denote the results at 0 K obtained from DFT calculations.

to 2.4 GPa and from 1.4 to 4.6 GPa, respectively. Based on the above findings, we could conclude that the elastic constants of both COF-1 and COF-5 decreased as the temperature decreased below specific thresholds. However, after the threshold temperature, the sensitivity of all the elastic constants to the temperature change became very different. This result indicates the difference in mechanisms for the thermally induced softening of 2D COFs at small and large temperatures, which will be explained in more detail later.

Based on the obtained elastic constants, we can further calculate the Young's modulus E of the monolayer COFs through the following formula:[58]

$$\frac{1}{E(\vec{a})} = \sum_{i,j,k,l=xy} a_i a_j a_k a_l S_{ijkl}, \quad \vec{a} = \begin{pmatrix} \cos(\varphi) \\ \sin(\varphi) \\ 0 \end{pmatrix} \quad 0 \le \varphi \le 2\pi, \quad (3)$$

where S_{ijkl} is the full second-order compliance tensor as defined above, $\vec{a}$ is the direction vector, and φ is the orientation angle in the plane.

It is worth noting that, like some other 2D materials with similar hexagonal structures, such as graphene, hexagonal-boron nitride (h-BN), and transition metal-dichalcogenides, the present 2D COFs also possessed two principal directions, *i.e.*, zigzag and armchair directions, as shown in Fig. 1d. In order to study the dependence of the Young's modulus on the crystalline orientation, we specifically evaluated here E in the zigzag and armchair directions by setting φ in eqn (3) as 0 and $\pi/2$, respectively. As for both COFs, the values of their E in the zigzag and armchair directions were close to each other, irrespective of the temperature (see Fig. 6). This result, to some extent, indicates the elastic isotropy of the monolayer COFs considered here. In terms of the thermal effect, its effect on the Young's modulus was exactly similar to that on the above elastic constants. Specifically, when the temperature was smaller than the critical value, *i.e.*, 60 K for COF-1 and 40 K for COF-5, the Young's moduli of COF-1 and COF-5 decreased from 28.5 GPa and 15.4 GPa to 6.6 GPa and 7.2 GPa, respectively. However, when the temperature was larger than the criti-

cal values, the Young's modulus became less sensitive to the temperature change, though it similarly decreased as the temperature grew. For instance, as the temperature further increased from the critical temperatures to 500 K, the Young's moduli of COF-1 and COF-5 were reduced from 6.6 GPa and 7.2 GPa to 2.9 GPa and 3.8 GPa, respectively.

A comparison of the Young's modulus of the present 2D COFs to the values of some other representative 2D materials with similar planar structures, such as graphene[40] and h-BN,[59] is illustrated in Table 2. In line with the method employed here, the Young's moduli of the monolayer graphene and h-BN shown here were similarly extracted from the strain-fluctuation method. As shown in Table 2, whether at the ground state (0 K) or room temperature (300 K), the Young's modulus of the 2D COFs was much lower than that of graphene and h-BN, denoting the high flexibility of the present 2D COFs. Meanwhile, as shown in Table S2,† we compared the Young's moduli of monolayer COF-5 obtained from the present NEP and previous all-atom optimized potentials for liquid simulations (OPLS-AA), which were developed specifically for liquid systems, such as peptides, proteins, nucleic acids, and organic solvents.[25,26] Although the accuracy of the Young's moduli in the armchair direction predicted from both potentials were very close to the result from the DFT calculations, the difference between the Young's moduli in the zigzag direction extracted from NEP and DFT calculations was only 2,6%, which was much smaller than the difference (56%) between

Table 2 A comparison of the Young's modulus of the present monolayer COFs to the values of some other 2D materials, including graphene[40] and h-BN.[59]

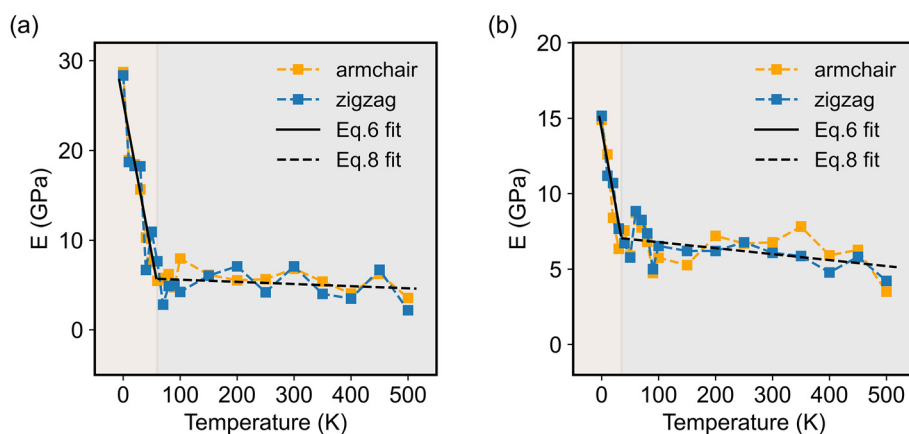| Material	Young's modulus (GPa)	
	0 K	300 K
Graphene[40]	939	424
h-BN[59]	723	180
COF-1	28.5	6.9
COF-5	15.4	6.4

Fig. 6 Young's moduli in the armchair and zigzag directions of (a) COF-1 and (b) COF-5 at different temperatures ranging from 0 to 500 K.

that calculated from OPLS-AA and DFT calculations. Moreover, the OPLS-AA predicted a strong mechanical anisotropy of COF-5, in contrast to the mechanical isotropy obtained from our NEP and DFT calculations. Thus, the present NEP is expected to provide higher levels of accuracy in estimating the elasticity of 2D COFs. Although the force field of OPLS-AA possesses parameters for a wide range of atoms and functional groups, it also needs to be specifically parameterized in the future for 2D COFs that contain some specific functional groups. The NEP developed here could serve as a benchmark for the future parameterization of the empirical potentials for 2D COFs.

Mechanism of the thermoelastic behaviors

Since the elastic properties of 2D materials are usually related to their configurations, taking monolayer COF-1 as an example, we illustrate its structures at two representative temperatures, *i.e.*, 10 K and 200 K, to explain the significant thermomechanical behaviors observed in monolayer COFs below the critical temperature. Fig. 7a and b show that serious thermal rippling existed in COF-1 at the temperature of 200 K, while COF-1 at the temperature of 10 K almost retained its original flatness configuration. Therefore, as illustrated in Fig. 7c, the expansion of monolayer COFs at relatively low temperatures was primarily resisted by the in-plane tensile stiffness, since it exhibited a planner configuration. However, as the temperature became higher, the de-rippling of the thermally rippled COFs by bending dominated their elongation now (Fig. 7d). As a monolayer material with atomic thickness, the monolayer COF usually possesses an extremely small bending stiffness. Thus, the thermally induced serious thermal rippling at a relatively high temperature was respon-

sible for the reduction in the elastic constants of the monolayer COFs at high temperatures. Actually, many previous MD simulation studies have pointed out that the out-of-plane thermal rippling in 2D materials exerts a notable influence on their elastic moduli.[40,60,61]

To better quantitatively measure the out-of-plane displacement of the monolayer COFs caused by the thermal rippling at different temperatures, we calculated the time-averaged RMS displacement $\bar{h}$ by using the following equation:

$$\bar{h} = \sqrt{\left\langle \sum_{i=1}^{N} \frac{w_i^2}{N} \right\rangle_t}, \quad (4)$$

where N is the total number of atoms and w_i is the out-of-plane displacement of the i-th atom. The RMS displacements together with the corresponding configurations of both COF-1 and COF-5 at the temperatures of 10, 50, and 200 K are shown in Fig. 8. The results for the structures at some other temperatures are presented in Fig. S6 and S7.† The results illustrate that as the temperature increased, both monolayer COF materials similarly exhibited a noticeable increase in the out-of-plane fluctuations. To further compare and analyze the out-of-plane fluctuations of COF-1 and COF-5, Fig. 9 presents a detailed depiction of their RMS displacements over the temperature range from 10 K to 500 K. The results consistently demonstrate that the degree of thermal rippling also correspondingly increased as the temperature rose within the temperature range considered in our MD simulations.

For a better understanding of the thermal rippling, we simplified the monolayer COF as a continuum 2D membrane. At a finite temperature, a membrane without any external forces can be fluctuated with both in-plane and out-of-plane modes.
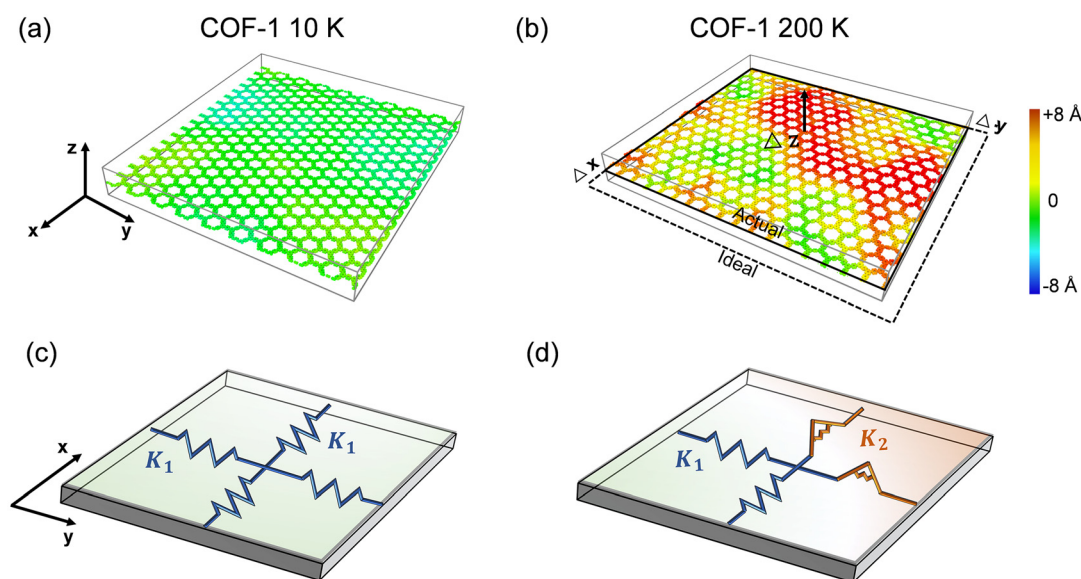

Fig. 7 The configurations of COF-1 monolayers at the temperatures of (a) 10 K and (b) 200 K. The contour illustrates an out-of-plane deformation. (c and d) The corresponding equivalent mechanical models of COF-1 at the temperatures of 10 K and 200 K. The planar COF is represented by an extension spring with the stiffness of K_1, while the rippled COF is represented by a torsion spring with the stiffness of K_2.
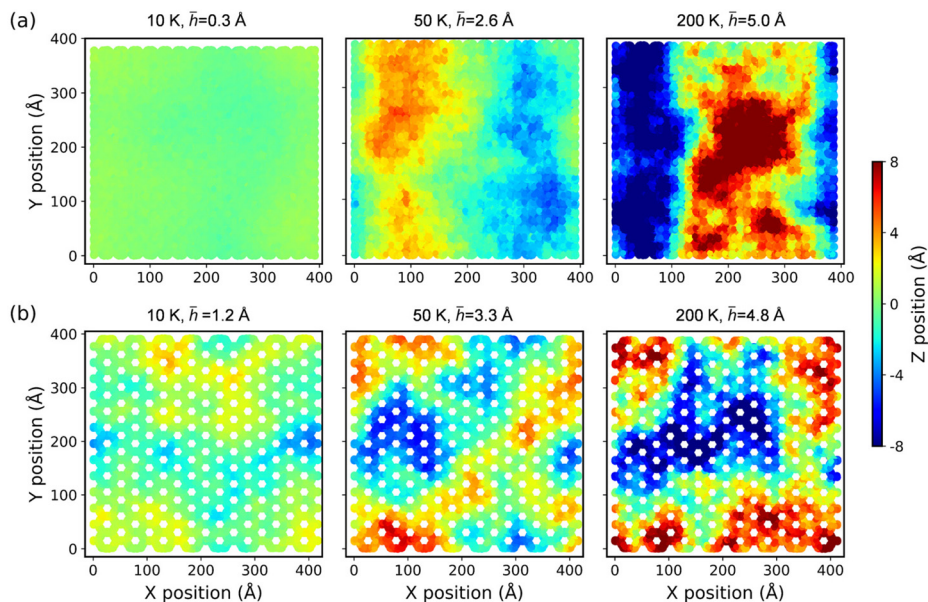
Fig. 8 The configurations of (a) COF-1 and (b) COF-5 monolayers at different temperatures. The contour illustrates an out-of-plane deformation of the COFs.
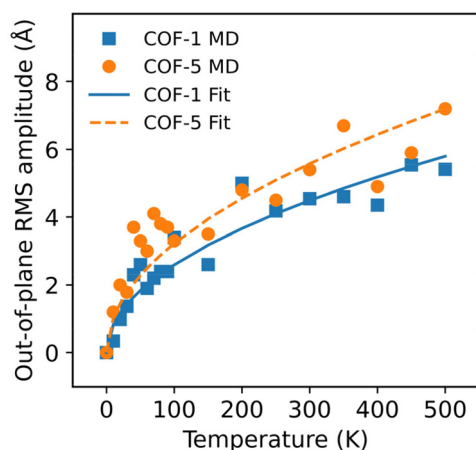

Fig. 9 The RMS amplitudes of the thermal rippling of COF-1 and COF-5 monolayers at different temperatures ranging from 10 to 500 K. The lines correspond to the results fitted by the model developed using statistical mechanics and thermodynamics.

The RMS amplitude of the out-of-plane fluctuation $\bar{h}$ of COFs below the critical temperature can be calculated according to the statistical mechanical analysis, which has the following expression:[60]

$$\bar{h} = \sqrt{\frac{L_0^2 k_B T \gamma_n}{16\pi^4 D}}, \tag{5}$$

where L_0 represents the size of the monolayer COFs, D denotes the bending stiffness, and γ_n is a dimensionless coefficient. We employed the above formula to fit the RMS displacements extracted from the MD simulations. As illustrated by the solid lines in Fig. 9, the theoretical model could well fit the MD

simulation results, which, to some extent, confirmed that the rippling of the monolayer COFs was indeed induced by the thermal fluctuation. Specifically, the fitting formulas were $\bar{h} = 0.26\sqrt{T}$ and $\bar{h} = 0.32\sqrt{T}$ for monolayer COF-1 and COF-5, respectively, indicating a smaller RMS displacement in COF-1. It could be noted that the difference in the fitting coefficients of COF-1 and COF-5 was due to their different bending stiffnesses, since both COFs considered in the MD simulations had similar dimensions. Theoretically, the COF-1 monolayer was expected to have a higher bending stiffness compared to COF-5 monolayer, as the COF-1 monolayer possessed a much denser structure.

We further extended the above theories to explain the thermally induced softening of the Young's modulus of the 2D COFs below the critical temperature, since the out-of-plane fluctuation now plays a dominant role in determining the elastic behaviors of monolayer 2D COFs.[60,62] According to the statistical mechanics and thermodynamics, the Young's modulus of monolayer COFs below the critical temperature can be expressed by the following formula:

$$E = E^* - \frac{E^* k_B T}{16\pi D}\left(\frac{4\pi^2 D}{E^* L_0^2} + \varepsilon_0\right)^{-1}, \tag{6}$$

where E^* is the Young's modulus at the ground state and ε_0 represents the residual strain. In *our* calculations, the moduli in two principal directions were averaged for the Young's modulus of both COF materials. As depicted in Fig. 6, the dependence of the Young's modulus on the temperature below the critical temperature could be well fitted by the above theoretical model for both 2D COFs. Remarkably, the values of E^* extracted from the curve fitting agreed well with the results directly obtained from the MD simulations.

Based on the analyses presented herein, the reduction in the elastic modulus of the 2D COFs at relatively low temperatures could be attributed to the synergistic interplay of the thermal rippling phenomenon and the well-established harmonic vibrations. As the temperature became higher, the impact of the anharmonic coupling between the bending and stretching modes tended to become more significant. As highlighted in an earlier theoretical study, such coupling can effectively mitigate the impact of the out-of-plane thermal fluctuations on the elastic modulus of 2D materials, thereby attenuating the observed softening effect.[60,63] In the current study, we conducted a parallel analysis to assess the impact of the anharmonic forces across different temperature regimes. Specifically, we computed the Grüneisen parameter of COF-1 and COF-5, which is a parameter with the ability to provide insights into the underlying anharmonic interactions of 2D COFs.[64] The Grüneisen parameter can be mathematically expressed as:[65,66]

$$\gamma = \frac{3\alpha B V_m}{C_v}, \tag{7}$$

where α is the linear thermal expansion coefficient, B is the bulk modulus, V_m is the molar volume, and C_v is the isometric heat capacity. Based on the values of α, B, and C_v evaluated from NEP-based MD simulations, in Fig. 10 we display the Grüneisen parameters for COF-1 and COF-5 at different temperatures. It could be found that at relatively low temperatures, the Grüneisen parameter of the monolayer 2D COFs was negative with a large magnitude. This large negative Grüneisen parameter of ZA modes is typically attributed to a significant membrane effect,[67] since, as revealed in the previous studies on various 2D materials, at low temperature the mainly excited phonon modes were the low-frequency acoustic modes that usually have a large negative Grüneisen parameter.[68,69] Therefore, the out-of-plane thermal fluctuations should have a dominant effect on the thermoelastic behaviors of monolayer

Fig. 10 Calculated temperature-dependent Grüneisen parameters for COF-1 and COF-5.

2D COFs below the critical temperature. As the temperature increased, the magnitude of the Grüneisen parameters significantly decreased, since high-frequency phonon modes with relatively small negative or positive Grüneisen parameters gradually get excited. This indicates that at high temperatures, the high-frequency phonon modes may have significant effects on the thermoelastic behaviors of monolayer 2D COFs.[68,69] Thus, above the critical temperature, the relationship between the Young's modulus and the temperature can be described by the well-known Wachtman relationship:[63,70]

$$E = E_0 - BT \exp\left(\frac{-T_0}{T}\right), \tag{8}$$

where B and T_0 are arbitrary constants and E_0 is the Young's modulus at absolute zero when the effect of the out-of-plane fluctuations is excluded. As shown in Fig. 6, the relationship between the Young's moduli of both 2D COFs and the temperature indeed could be well fitted by the Wachtman's equation above the critical temperatures. Moreover, through the curve fitting, T_0 was found to be approximately 0.1 K. Thus, considering $T \gg T_0$, eqn (7) can be simplified into $E = E_0 + BT_0 - BT$, which further proves a linear relationship between the Young's modulus and the temperature above the critical temperature as observed in the MD simulations.

Summary and conclusions

In summary, we developed an NEP model-based MLP for accurately evaluating the thermoelastic properties of two classical monolayer 2D COFs (COF-1 and COF-5). Through comparing with the results obtained from DFT calculations, the MLP trained here was proven to have the capability to enable one to study the elastic behaviors of monolayer COFs, offering greatly improved computational efficiency and high accuracy. Thus, the trained MLP was further employed in MD simulations to calculate the elastic constants of monolayer COFs with relatively large sizes and at high temperatures, as implemented by the strain-fluctuation method. The elasticity of both COF-1 and COF-5 was found to be almost isotropic, irrespective of the temperature. However, the elastic moduli of both monolayer COFs significantly dependent on the temperature, and were found to decrease as the temperature increased. Moreover, the temperature sensitivity of the elastic modulus was found to decrease after a critical temperature, e.g., ~60 K for COF-1 and ~40 K for COF-5, because different thermoelastic mechanisms dominated before and after the critical temperature. Specifically, the thermoelastic behavior could be majorly ascribed to the thermal rippling effect before the critical temperature, while the damping effect of anharmonic vibrations became the dominant mechanism after the critical temperature. Based on these mechanisms, two analytical models were also proposed for the temperature dependence of the elastic modulus before and after the critical temperature, which were found to fit the MD simulation results well. The present study not only offers a precise potential for describing the thermoe-
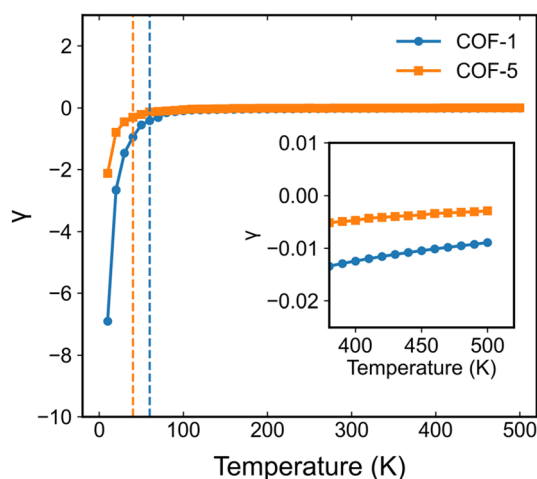
lastic behaviors of monolayer COFs but also provides valuable insights into the elastic properties of 2D COFs in realistic situations.

Finally, the following efforts can be made to further extend the application of the NEP in the study of the mechanical properties of 2D COFs. In addition to the monolayer 2D COFs studied here, multilayer structures of 2D COFs also widely exist, which have a wide range of applications.[71,72] To develop MLPs for multilayer 2D COFs, the present approach can be further expanded by integrating inter-layer interactions and different stacking methods into the training process of the NEP. Besides, in addition of the elastic property, the fracture property is also of importance for the mechanical performance of 2D COFs. To simulate the fracture behaviors of 2D COFs with large deformations, some representative structures of 2D COFs during the entire tension process need to be added to the current training sets.

Associated content

The training and testing results for the NEP models are freely available at **https://github.com/bing93wang/COF-NEP/**.

Conflicts of interest

There are no conflicts to declare.

Acknowledgements

References

1 A. P. Côté, A. I. Benin, N. W. Ockwig, M. O'Keeffe, A. J. Matzger and O. M. Yaghi, *Science*, 2005, **310**, 1166–1170.

2 H. Furukawa and O. M. Yaghi, *J. Am. Chem. Soc.*, 2009, **131**, 8875–8883.

3 J. Fu, S. Das, G. Xing, T. Ben, V. Valtchev and S. Qiu, *J. Am. Chem. Soc.*, 2016, **138**, 7673–7680.

4 X. Guan, Y. Ma, H. Li, Y. Yusran, M. Xue, Q. Fang, Y. Yan, V. Valtchev and S. Qiu, *J. Am. Chem. Soc.*, 2018, **140**, 4494–4498.

5 H. Li, Q. Pan, Y. Ma, X. Guan, M. Xue, Q. Fang, Y. Yan, V. Valtchev and S. Qiu, *J. Am. Chem. Soc.*, 2016, **138**, 14783–14788.

6 S. Yan, X. Guan, H. Li, D. Li, M. Xue, Y. Yan, V. Valtchev, S. Qiu and Q. Fang, *J. Am. Chem. Soc.*, 2019, **141**, 2920–2924.

7 Q. Fang, S. Gu, J. Zheng, Z. Zhuang, S. Qiu and Y. Yan, *Angew. Chem., Int. Ed.*, 2014, **53**, 2878–2882.

8 A. M. Evans, A. Giri, V. K. Sangwan, S. Xun, M. Bartnof, C. G. Torres-Castanedo, H. B. Balch, M. S. Rahn, N. P. Bradshaw, E. Vitaku, D. W. Burke, H. Li, M. J. Bedzyk, F. Wang, J.-L. Brédas, J. A. Malen, A. J. H. McGaughey, M. C. Hersam, W. R. Dichtel and P. E. Hopkins, *Nat. Mater.*, 2021, **20**, 1142–1148.

9 Y. Zhang, J. Duan, D. Ma, P. Li, S. Li, H. Li, J. Zhou, X. Ma, X. Feng and B. Wang, *Angew. Chem., Int. Ed.*, 2017, **56**, 16313–16317.

10 D. A. Vazquez-Molina, G. S. Mohammad-Pour, C. Lee, M. W. Logan, X. Duan, J. K. Harper and F. J. Uribe-Romo, *J. Am. Chem. Soc.*, 2016, **138**, 9767–9770.

11 S. Das, P. Heasman, T. Ben and S. Qiu, *Chem. Rev.*, 2017, **117**, 1515–1563.

12 R. Liang, S. Jiang, R. A and X. Zhao, *Chem. Soc. Rev.*, 2020, **49**, 3920–3951.

13 Y. Jin, Y. Hu and W. Zhang, *Nat. Rev. Chem.*, 2017, **1**, 0056.

14 A. M. Evans, M. R. Ryder, N. C. Flanders, E. Vitaku, L. X. Chen and W. R. Dichtel, *Ind. Eng. Chem. Res.*, 2019, **58**, 9883–9887.

15 L. Zhu, Y. Jin, Q. Xue, X. Li, H. Zheng, T. Wu and C. Ling, *J. Mater. Chem. A*, 2016, **4**, 15015–15021.

16 W. Li, Y. Yang, J. K. Weber, G. Zhang and R. Zhou, *ACS Nano*, 2016, **10**, 1829–1835.

17 S. Thakur and A. Giri, *J. Mater. Chem. A*, 2023, **11**, 18660–18667.

18 S. Thakur and A. Giri, *Mater. Horiz.*, 2023, **10**, 5484–5491.

19 Y. Yang, Y. Xu, Q. Li, Y. Zhang and H. Zhou, *J. Mater. Chem. A*, 2022, **10**, 19444–19465.

20 Z. Wang, Q. Yu, Y. Huang, H. An, Y. Zhao, Y. Feng, X. Li, X. Shi, J. Liang, F. Pan, P. Cheng, Y. Chen, S. Ma and Z. Zhang, *ACS Cent. Sci.*, 2019, **5**, 1352–1359.

21 Q. Fang, Z. Pang, Q. Ai, Y. Liu, T. Zhai, D. Steinbach, G. Gao, Y. Zhu, T. Li and J. Lou, *Proc. Natl. Acad. Sci. U. S. A.*, 2023, **120**, e2208676120.

22 C. Ding, M. Breunig, J. Timm, R. Marschall, J. Senker and S. Agarwal, *Adv. Funct. Mater.*, 2021, **31**, 2106507.

23 P. Kapri, T. Kawakami and M. Koshino, *Comput. Mater. Sci.*, 2023, **228**, 112282.

24 J. Zhang, *Phys. Chem. Chem. Phys.*, 2018, **20**, 29462–29471.

25 H. Li and J.-L. Brédas, *Chem. Mater.*, 2021, **33**, 4529–4540.

26 W. L. Jorgensen, D. S. Maxwell and J. Tirado-Rives, *J. Am. Chem. Soc.*, 1996, **118**, 11225–11236.

27 W. Hao, Y. Zhao, L. Miao, G. Cheng, G. Zhao, J. Li, Y. Sang, J. Li, C. Zhao, X. He, C. Sui and C. Wang, *Nano Lett.*, 2023, **23**, 1416–1423.

28 P. H. H. Duong, Y. K. Shin, V. A. Kuehl, M. M. Afroz, J. O. Hoberg, B. Parkinson, A. C. T. van Duin and K. D. Li-Oakey, *ACS Appl. Mater. Interfaces*, 2021, **13**, 42164–42175.

29 B. Mortazavi, X. Zhuang, T. Rabczuk and A. V. Shapeev, *Mater. Horiz.*, 2023, **10**, 1956–1968.

30 B. Mortazavi, B. Javvaji, F. Shojaei, T. Rabczuk, A. V. Shapeev and X. Zhuang, *Nano Energy*, 2021, **82**, 105716.

31 B. Mortazavi, E. V. Podryabinkin, I. S. Novikov, T. Rabczuk, X. Zhuang and A. V. Shapeev, *Comput. Phys. Commun.*, 2021, **258**, 107583.

32 B. Mortazavi, M. Silani, E. V. Podryabinkin, T. Rabczuk, X. Zhuang and A. V. Shapeev, *Adv. Mater.*, 2021, **33**, 2102807.

33 P. Ying, H. Dong, T. Liang, Z. Fan, Z. Zhong and J. Zhang, *Extreme Mech. Lett.*, 2023, **58**, 101929.

34 Z. Fan, Z. Zeng, C. Zhang, Y. Wang, K. Song, H. Dong, Y. Chen and T. Ala-Nissila, *Phys. Rev. B*, 2021, **104**, 104309.

35 M. Parrinello and A. Rahman, *J. Chem. Phys.*, 1982, **76**, 2662–2666.

36 S. M. J. Rogge, M. Waroquier and V. Van Speybroeck, *Acc. Chem. Res.*, 2018, **51**, 138–148.

37 X. Li, P. Yadav and K. P. Loh, *Chem. Soc. Rev.*, 2020, **49**, 4835–4866.

38 S. Kim and H. C. Choi, *ACS Omega*, 2020, **5**, 948–958.

39 J. F. Dienstmaier, A. M. Gigler, A. J. Goetz, P. Knochel, T. Bein, A. Lyapin, S. Reichlmaier, W. M. Heckl and M. Lackinger, *ACS Nano*, 2011, **5**, 9737–9745.

40 S. Thomas, K. M. Ajith, S. U. Lee and M. C. Valsakumar, *RSC Adv.*, 2018, **8**, 27283–27292.

41 A. Stukowski, *Modell. Simul. Mater. Sci. Eng.*, 2010, **18**, 015012.

42 P. H. Hünenberger, in *Advanced Computer Simulation*, Springer Berlin Heidelberg, Berlin, Heidelberg, 2005, pp. 105–149.

43 G. Kresse and J. Furthmüller, *Phys. Rev. B: Condens. Matter Mater. Phys.*, 1996, **54**, 11169–11186.

44 G. Kresse and D. Joubert, *Phys. Rev. B: Condens. Matter Mater. Phys.*, 1999, **59**, 1758–1775.

45 J. P. Perdew, K. Burke and M. Ernzerhof, *Phys. Rev. Lett.*, 1996, **77**, 3865–3868.

46 Z. Fan, Y. Wang, P. Ying, K. Song, J. Wang, Y. Wang, Z. Zeng, K. Xu, E. Lindgren, J. M. Rahm, A. J. Gabourie, J. Liu, H. Dong, J. Wu, Y. Chen, Z. Zhong, J. Sun, P. Erhart, Y. Su and T. Ala-Nissila, *J. Chem. Phys.*, 2022, **157**, 114801.

47 Z. Fan, W. Chen, V. Vierimaa and A. Harju, *Comput. Phys. Commun.*, 2017, **218**, 10–16.

48 J. R. Ray, *J. Appl. Phys.*, 1982, **53**, 6441–6443.

49 K. Yoshimoto, G. J. Papakonstantopoulos, J. F. Lutsko and J. J. de Pablo, *Phys. Rev. B: Condens. Matter Mater. Phys.*, 2005, **71**, 184108.

50 M. Bernetti and G. Bussi, *J. Chem. Phys.*, 2020, **153**, 114107.

51 A. Giri and P. E. Hopkins, *Nano Lett.*, 2021, **21**, 6188–6193.

52 A. Giri, A. M. Evans, M. A. Rahman, A. J. H. McGaughey and P. E. Hopkins, *ACS Nano*, 2022, **16**, 2843–2851.

53 T. P. Kaloni, Y. C. Cheng and U. Schwingenschlögl, *J. Appl. Phys.*, 2013, **113**, 104305.

54 V. Wang, N. Xu, J.-C. Liu, G. Tang and W.-T. Geng, *Comput. Phys. Commun.*, 2021, **267**, 108033.

55 Y. Le Page and P. Saxe, *Phys. Rev. B: Condens. Matter Mater. Phys.*, 2001, **63**, 174103.

56 W. Li, H. Kou, X. Zhang, J. Ma, Y. Li, P. Geng, X. Wu, L. Chen and D. Fang, *Mech. Mater.*, 2019, **139**, 103194.

57 D. Zakarian, A. Khachatrian and S. Firstov, *Met. Powder Rep.*, 2019, **74**, 204–206.

58 S. Yalameha, Z. Nourbakhsh and D. Vashaee, *Comput. Phys. Commun.*, 2022, **271**, 108195.

59 S. Thomas, K. M. Ajith and M. C. Valsakumar, *Superlattices Microstruct.*, 2017, **111**, 360–372.

60 W. Gao and R. Huang, *J. Mech. Phys. Solids*, 2014, **66**, 42–58.

61 H. Li and J.-L. Brédas, *J. Phys. Chem. Lett.*, 2018, **9**, 4215–4220.

62 W. Helfrich and R.-M. Servuss, *Il Nuovo Cimento D*, 1984, **3**, 137–151.

63 O. L. Anderson, *Phys. Rev.*, 1966, **144**, 553–557.

64 B. Peng, H. Zhang, H. Shao, Y. Xu, X. Zhang and H. Zhu, *RSC Adv.*, 2016, **6**, 5767–5773.

65 G. Grimvall, *Thermophysical Properties of Materials*, North-Holland, Oxford, England, 2nd edn, 1999.

66 X. Tan, H. Shao, T. Hu, G. Liu, J. Jiang and H. Jiang, *Phys. Chem. Chem. Phys.*, 2015, **17**, 22872–22881.

67 P. Anees, M. C. Valsakumar and B. K. Panigrahi, *Phys. Chem. Chem. Phys.*, 2017, **19**, 10518–10526.

68 Q. Li, J. Zhou, G. Liu and X. G. Wan, *Carbon*, 2022, **187**, 349–353.

69 G. Liu and J. Zhou, *J. Phys.: Condens. Matter*, 2019, **31**, 065302.

70 R. J. Bruls, H. T. Hintzen, G. de With and R. Metselaar, *J. Eur. Ceram. Soc.*, 2001, **21**, 263–268.

71 S. Chandra, S. Kandambeth, B. P. Biswal, B. Lukose, S. M. Kunjir, M. Chaudhary, R. Babarao, T. Heine and R. Banerjee, *J. Am. Chem. Soc.*, 2013, **135**, 17853–17861.

72 W. Zhou, M. Wei, X. Zhang, F. Xu and Y. Wang, *ACS Appl. Mater. Interfaces*, 2019, **11**, 16847–16854.